

Timing resolution from very thin LGAD sensors tested on particle beam down to 12 ps

Robert Stephen White^a, Marco Ferrero^a, Valentina Sola^{b,a}, Anna Rita Altamura^{b,a}, Roberta Arcidiacono^{c,a}, Maurizio Boscardin^{d,e}, Nicolò Cartiglia^a, Matteo Centis Vignali^{d,e}, Tommaso Croci^f, Matteo Durando^b, Simone Galletto^b, Alessandro Fondacci^f, Leonardo Lanteri^{b,a}, Luca Menzio^{c,a}, Francesco Moscatelli^{f,g}, Giovanni Paternoster^{d,e}, Federico Siviero^a

^a*Istituto Nazionale di Fisica Nucleare, Sezione di Torino, via P. Giuria 1, Torino, Italy*

^b*Università degli Studi di Torino, via P. Giuria 1, Torino, Italy*

^c*Università del Piemonte Orientale, largo Donegani 2, Novara, Italy*

^d*Fondazione Bruno Kessler, via Sommarive 18, Povo, Trento, Italy*

^e*Trento Institute for Fundamental Physics and Applications, via Sommarive 14, Povo, Trento, Italy*

^f*Istituto Nazionale di Fisica Nucleare, Sezione di Perugia, via A. Pascoli, Perugia, Italy*

^g*Consiglio Nazionale delle Ricerche, Istituto Officina dei Materiali, via A. Pascoli, Perugia, Italy*

Abstract

The paper reports on the timing resolution obtained with the Low-Gain Avalanche Diode (LGAD) sensors for extreme fluences at the DESY Test Beam Facility with 4 GeV/c electrons. The LGADs adopt an n -in- p technology with a p^+ -type boron gain implant, co-implanted with carbon to mitigate acceptor deactivation. The substrate thickness of the sensors varies from 20 μm to 45 μm , with an active area spanning from 0.75×0.75 to 1.28×1.28 mm^2 . A set of 30 μm sensors irradiated with neutrons at fluences between 4×10^{14} and 2.5×10^{15} $\text{n}_1 \text{ MeV eq. cm}^{-2}$ were tested on the beam. The gain was measured between 7 and 40 across all non-irradiated sensors in the study, and between 7 and 30 in irradiated sensors. The experimental setup consisted of a 45 μm -thick trigger sensor with an active area of 3.6×3.6 mm^2 , four device-under-test (DUT) planes, and a Photonis micro-channel plate photomultiplier tube (MCP) as a time reference. The timing resolution was calculated from Gaussian fitting of the difference in times of arrival of a particle at a DUT and the MCP, using the constant fraction discrimination technique. A timing resolution of 26.4 ps was achieved in

45 μm sensors, and down to 16.6 ps in 20 μm sensors. The combination of two 20 μm LGAD sensors reached a timing resolution of 12.2 ps. A timing resolution of below 20 ps was obtained in all irradiated 30 μm sensors.

Keywords: Solid State Radiation Sensors; Thin LGAD Sensors; Radiation Hardness; Precision Timing

1. Introduction

Future High-Energy Physics (HEP) experiments are expected to reach significantly higher instantaneous luminosities and, therefore, will require detectors that can operate in extreme fluence conditions. In the CERN High-Luminosity Large Hadron Collider (HL-LHC), the innermost tracking layers of the high energy detectors, A Toroidal LHC Apparatus (ATLAS) and Compact Muon Solenoid (CMS), will be exposed to a fluence of $3.5 \times 10^{16} \text{ n}_{1 \text{ MeV eq. cm}^{-2}}$ [1, 2], while in the Future Circular Collider (FCC-hh), this is expected to reach $\sim 6 \times 10^{16} \text{ n}_{1 \text{ MeV eq. cm}^{-2}}$ during proton-proton collisions [3, 4].

Low-Gain Avalanche Photodiode (LGAD) technology is at the forefront of future detectors, due to its superior timing resolution and radiation hardness [5]. Current LGAD technology can achieve a temporal resolution between 25 and 35 ps depending on substrate thickness (sub-55 μm) [6], and can survive in high radiation environments up to $\sim 2 \times 10^{15} \text{ n}_{1 \text{ MeV eq. cm}^{-2}}$ while returning a modest gain [7].

The LGAD sensors used in the analysis have been designed to investigate how thin substrates respond to irradiation to the extreme fluences (EXFLU), and how timing resolution and gain, among other properties, evolve with substrate thickness and irradiation fluence. Two batches of sensors manufactured by the Fondazione Bruno Kessler (FBK) were employed. The EXFLU0 sensors have the same layout and gain implant design as the UFSD3.2 sensor produced at FBK, but on thinner substrates, namely 25 and 35 μm . While EXFLU1 sensors have a dedicated sensor layout, with optimised peripheral structures, and further explore the beneficial effects derived from thin substrates, down to 15 μm . The sensors were irradiated with neutrons in the TRIGA Mark II research nuclear reactor at the Jozef Stefan Institute [8]. The characterisation and performance of EXFLU sensors, both before and after irradiation, were completed at the laboratory in Turin, and are reported in [9, 10, 11, 12].

This paper reports on the performance of the EXFLU sensors at the Test Beam Facility at DESY [13]. The EXFLU design is described in detail in Section 2. The experimental setup and the approaches to data acquisition and signal analysis are explained in Section 3. The timing resolution measurements are presented for both non-irradiated and irradiated samples in Section 4. Conclusions on the timing performance of the EXFLU sensors are drawn in Section 5.

2. The EXFLU LGAD Design

The LGAD design comprises of a silicon pixel sensor with a very thin substrate of thickness $\sim 50\text{ }\mu\text{m}$ implanted with a gain layer $\sim 1\text{ }\mu\text{m}$ beneath the surface with an intrinsic gain of ~ 20 . These finely segmented pixel sensors can precisely measure the position and timing of a hit simultaneously in the ATLAS and CMS detectors, with a target precision of $\sim 30\text{ ps}$ timing resolution and $\sim 10\text{ }\mu\text{m}$ spatial resolution.

In this study, *n*-in-*p* LGADs with a *p*-type bulk concentration of approximately $10^{12}\text{ at cm}^{-3}$ are used. The gain implant is boron-doped with a carefully tuned peak *p*⁺-type concentration of $\sim 10^{16}\text{ at cm}^{-3}$ at a depth between ~ 0.5 and $2\text{ }\mu\text{m}$ within the substrate, illustrated in Fig. 1. A carbon co-implant is also injected into the gain layer to mitigate the electronic deactivation of boron acceptors due to the effects of irradiation [14, 15].

Implantation and thermal activation of the carbon and boron acceptors to synthesise the gain layer adhere to two different schemes: low-carbon, low-boron diffusion (CBL), and high-carbon, low-boron diffusion (CHBL). The CBL mode incurs implanting carbon and boron together before simultaneous thermal activation at low temperature. The CHBL scheme involves implantation and activation of carbon under a high heat load, followed by implantation and activation of boron at a lower temperature. Carbon-boron inactivation effects emerge during thermal activation, and more strongly manifest in CBL than CHBL implantation [16, 17].

The EXFLU0 batch of sensors was implanted under the CHBL mode. A single-pad (SP) device measures $1.28 \times 1.28\text{ mm}^2$ at the surface, while the dual-pad LGAD-PIN (LP) device measures $1.0 \times 1.0\text{ mm}^2$ on each pad.

The EXFLU1 batch of sensors differ to the EXFLU0 batch in primarily in implantation mode, geometry, and periphery design. The EXFLU1 sensors were implanted under the CBL mode with the exception of one $20\text{ }\mu\text{m}$ -thick design. The $20\text{ }\mu\text{m}$ EXFLU1 sensor under CBL implantation has a higher *p*⁺

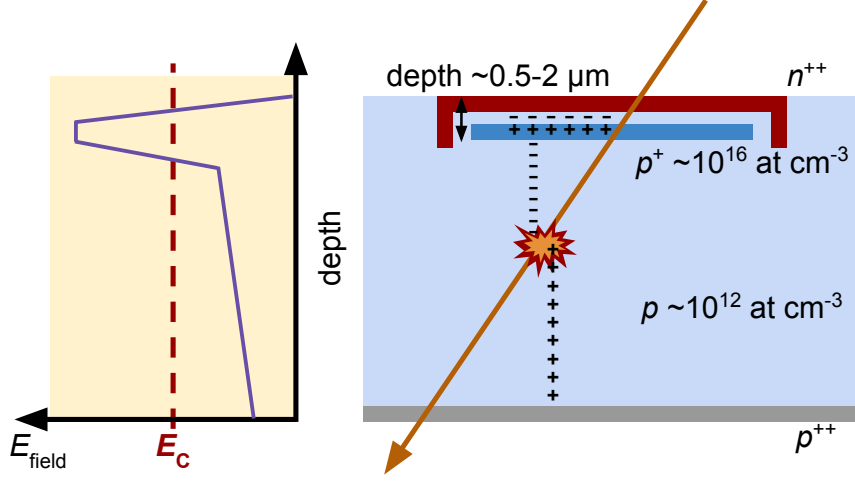
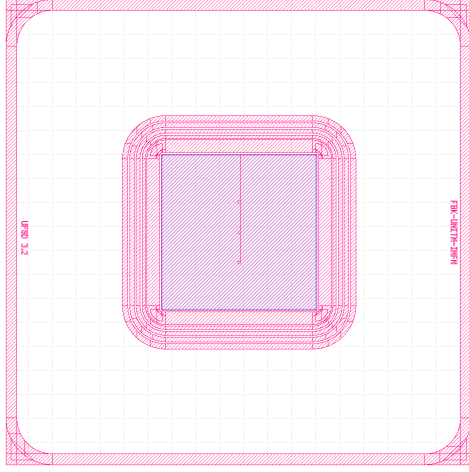


Figure 1: Specifications for the LGAD sensors studied: an n -in- p design with a peak boron (p^+ -type) doping concentration of $\sim 10^{16}$ at cm^{-3} in the gain implant.

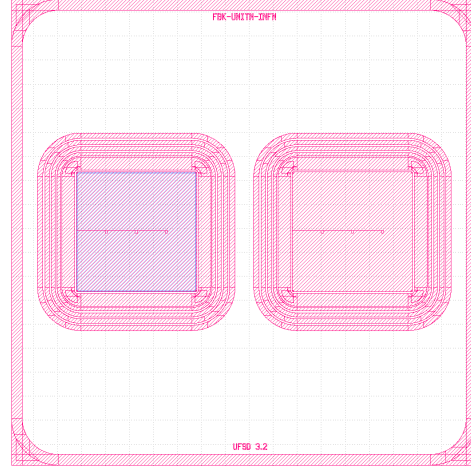
dose than the CHBL-activated sensor of the same thickness. The measurable consequence of inactivation and the difference in p^+ dose in for the EXFLU1 sensors is the prolongation of sensor bulk depletion under an external reverse bias. The SP geometry is identical across EXFLU batches, while the EXFLU1 LP device has a smaller active area, measuring $0.75 \times 0.75 \text{ mm}^2$ on each pad. The difference in periphery design results in a slightly lower bulk breakdown voltage on average for EXFLU0 sensors for a given thickness, but produce comparable results for the purposes of the timing study. The EXFLU0 and EXFLU1 schematics for both SP and LP devices are illustrated in Fig. 2.

The nominal thicknesses of the sensors studied at the Test Beam Facility range from 15 to 45 μm . The effective active thickness is therefore considered to be the nominal thickness minus 2 μm for the LGADs. Considering the capacitance of each sensor by using a parallel plate approximation, the LP device was used for sensors with active thickness less than 35 μm . This ensures that the sensor capacitance is maintained below 5 pF after full sensor depletion.

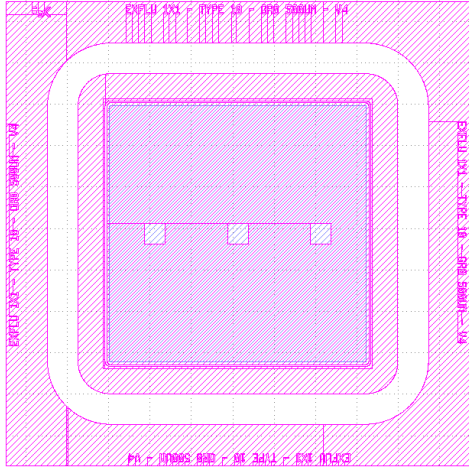
The sensors of larger active thickness have a much lower bulk concentration, p_{bulk} , than in thinner substrates. The p_{bulk} of sensors of thickness less than 30 μm is $1.5 \times 10^{14} \text{ cm}^{-3}$, for the 30 μm sensors is $1.5 \times 10^{13} \text{ cm}^{-3}$,



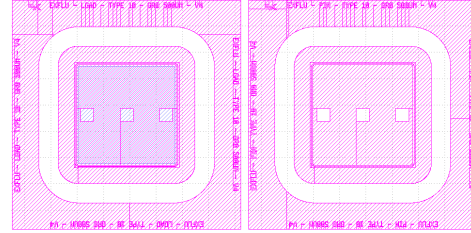
(a) EXFLU0 SP



(b) EXFLU0 LP



(c) EXFLU1 SP



(d) EXFLU1 LP

Figure 2: Schematic images of EXFLU SP and LP devices used for timing performance studies: the EXFLU0 SP (a) and LP (b) devices with an active area of $1.28 \times 1.28 \text{ mm}^2$ and $1.0 \times 1.0 \text{ mm}^2$ per pad, respectively, and the EXFLU1 SP (c) and LP (d) devices with an active area of $1.28 \times 1.28 \text{ mm}^2$ and $0.75 \times 0.75 \text{ mm}^2$ per pad, respectively.

Table 1: The design specifications and device types tested, with relative peak gain layer doping concentration, implantation mode, p_{bulk} , device type, and sensor capacitance. The EXFLU0 sensors are demarcated as the 35 and 25 μm substrates, while the EXFLU1 samples correspond to the 45, 30, and 20 μm substrates. The p^+ dose is normalised to the FBK reference value. All sensors have a C co-implantation of value 1.0, following Ref. [17].

Thick. [μm]	p^+ dose	Diffusion	p_{bulk} [cm^{-3}]	DUT	C_{DUT} [pF]
35	0.94	CHBL	$<5 \times 10^{12}$	SP	4.8
25	0.94	CHBL	1.5×10^{14}	LP	4.1
45	1.14	CBL	$<5 \times 10^{12}$	SP	3.9
30	1.12	CBL	1.5×10^{13}	LP	1.9
20	0.80	CHBL	1.5×10^{14}	LP	2.9
20	0.96	CBL	1.5×10^{14}	LP	2.9

and for thickness greater than 30 μm is about $5 \times 10^{12} \text{ cm}^{-3}$ or below.

The design specifications, including the p^+ relative dose (normalised to the FBK reference dose and expressed in arbitrary units), p_{bulk} , the devices tested, and the pad capacitance are summarised in Table 1. In all sensors studied, a carbon dose of 1.0 is co-implanted according to Ref. [17].

At least one non-irradiated sensor of each thickness was tested at the Test Beam Facility. A single CHBL and CBL 20 μm sensor was tested in this case. EXFLU1 30 μm sensors irradiated to the fluences of 4×10^{14} , 8×10^{14} , 1.5×10^{15} , and $2.5 \times 10^{15} \text{ n}_1 \text{ MeV eq. cm}^{-2}$ have been tested on beam. All measurements on the irradiated sensors were performed after annealing at 60°C for 80 minutes [18].

The EXFLU1 sensors are well established as having the best acceptor-removal mitigation performance of any very thin LGAD produced by FBK to date [11, 12]. The irradiated sensors used for this timing study have demonstrated that, when operated at higher biases, the gain performance observed in the non-irradiated sensors can be reproduced up to a fluence of $2.5 \times 10^{15} \text{ n}_1 \text{ MeV eq. cm}^{-2}$ [14].

3. EXFLU operations at the DESY Test Beam Facility

Each sensor sample was read out using a single-channel Santa Cruz (SC) board configured with a 470Ω inverting transimpedance amplifier integrated with an Infineon SiGe RF transistor, capable of supporting bandwidths of

$\mathcal{O}(10\text{ GHz})$ while providing low noise and high gain [17]. An external amplification stage is incorporated using a commercial low-noise Cividec C1 broadband amplifier with 2 GHz bandwidth and 20 dB gain. Data acquisition was performed using an eight-channel Lecroy WaveRunner 8208HD oscilloscope, with a 10 GSa/s sampling rate and 2 GHz bandwidth. The overall system bandwidth, BW_{tot} , is $\sim 1.4\text{ GHz}$, corresponding to a limit on the measureable inverted signal rise time $t_{\text{rise}} = 0.35/BW_{\text{tot}}$ of 250 ps. The sensors selected for the timing study are not limited by the bandwidth, nor is the minimum measurable t_{rise} reached for the thinnest sensor substrates.

The timing resolution campaign was performed at the DESY Test Beam Facility. The electron beam momentum was set to 4 GeV/c, resulting in a particle rate of 1.0 kHz/cm⁻². The rate is recorded at the facility's beam monitor, and can be an underestimate of the effective rate.

Two different apparatuses were used, one for non-irradiated DUTs and the other for irradiated ones. The former operates at ambient temperature, which for the Test Beam Facility was constantly at 18°C during the testing campaign. The latter uses a polythene cold box filled with solidified CO₂ to maintain an operating temperature as low as -50°C, monitored using an Arduino data logger.

Each apparatus is set up with a series of three parallel SC boards mounted with sensors for DAQ, in the following order of beam incidence: a 45 μm trigger sensor with active area $3.6 \times 3.6\text{ mm}^2$, operated at 230 V in the non-irradiated DUT setup and at 140 V in the irradiated DUT setup, taking into account the different temperature of operation, with a minimum inverted signal threshold of 40 mV; the first DUT, DUT 1; the second DUT, DUT 2, of the same thickness as DUT 1; and a Photonis micro-channel plate photo-multiplier tube (MCP) used as a timing reference. The DUTs were read out simultaneously with the trigger and MCP during DAQ for each run. The intrinsic timing resolution of the MCP was calculated at $5 \pm 2\text{ ps}$ using the data taken with 20 μm sensors, as outlined in Section 3.2. The coincidence between the trigger sensor and MCP yielded a 97% geometric efficiency.

For each DUT bias point, a data acquisition (DAQ) stopping condition of at least 30,000 trigger events was required, equal to about 40 minutes of data taking per DUT bias point. This corresponds to a coincidence rate of signal events between the DUT and the MCP of between 3.4 and 12.7%, depending on the sensor geometry. Across all bias points for a given DUT, DAQ was performed for up to 8 hours continuously. A temperature variation was therefore observed, between -50 and -42°C according to the Arduino, due

to ambient heating during DAQ.

The operating conditions of EXFLU sensors are suited for timing performance analysis. The external bias corresponding to bulk breakdown due to gain in each sample lies within a range of 100 V and 250 V, as shown in Fig 3. The range of bias points applied to the DUTs during data taking is selected at varying intervals from a bulk electric-field strength of at least $3 \text{ V}\mu\text{m}^{-1}$ to the DUT breakdown. The lower bias threshold corresponds to the point at which the electron drift velocity is saturated. This ensures a good separation between the amplitude of signal and noise events, demonstrated in Fig 4 for the $20 \mu\text{m}$ CBL-mode LGAD sensor operated under 150 V bias at 18°C . In this example, the region of signal events is situated above amplitudes of 25 mV. The shape of this distribution is typical of the data collected for almost all EXFLU samples: the noise peak width is mostly constant until near the breakdown of the sensor, while the distribution of signal events broadens, with a higher average amplitude, and separates more clearly from noise events under higher biases. The noise in the $45 \mu\text{m}$ sample was very large with respect to the noise observed in other samples during DAQ. For the $45 \mu\text{m}$ samples, results are substituted with data of lower background noise obtained using a $45 \mu\text{m}$ sensor and a ^{90}Sr β source, with activity 37 kBq, at 18°C . Only events with electrons of 2.28 MeV energy are recorded with this source, so events are MIP-like during DAQ. Therefore a single-plane setup is used, with the MCP as the trigger and timing reference, due to the significantly lower energy and flux of ionising particles emitted by the β source.

The breakdown trends for irradiated sensors are obtained from measuring the leakage current with increasing reverse bias at -20°C . This is necessary due to the increase in leakage current induced by irradiation, and so mitigates early breakdown. The irradiated $30 \mu\text{m}$ sensors operate at higher biases than the non-irradiated sample, between 200 and 400 V. The breakdown point of each sensor increases with the level of irradiation, highlighted in Fig. 5. The single-event burnout (SEB) limit for a $30 \mu\text{m}$ -thick substrate is 405 V, considering a maximum electric-field strength of $13.5 \text{ V}\mu\text{m}^{-1}$ [19]. The acceptor removal coefficient in $30 \mu\text{m}$ EXFLU1 sensors was estimated at $1.22 \pm 0.10 \times 10^{-16} \text{ cm}^2 \text{ n}_{1 \text{ MeV eq.}}^{-1}$ [12], and is the most radiation-hard gain implant design produced by FBK to date.

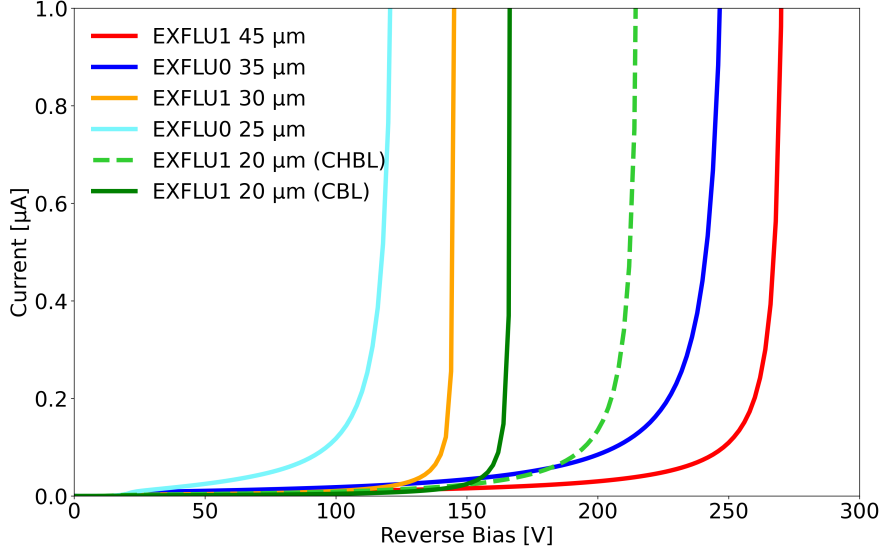


Figure 3: The breakdown trends for the non-irradiated EXFLU samples. The two 20 μm EXFLU1 sensors differ by gain implantation method, with the CHBL mode leading to a higher breakdown voltage.

3.1. Signal analysis

The charge injected within the sensor is calculated from the fit of a Landau-plus-Gaussian convolution to the distribution of signal area. The typical charge measured in the non-irradiated samples ranges from 2 to 8 fC for sensors thinner than 30 μm , increasing up to 10 fC for the 30 μm sensors, and 15 fC for the 35 μm sensors, as shown in Fig 6. The signal gain is given by the fraction of charge injected into an LGAD and into a PIN of identical substrate thickness and area, i.e. an identical device in the absence of a gain implant. Following Ref. [20], the charge deposition for the PIN sensor can be estimated, and hence the gain for each sensor is extracted using the effective substrate thickness, and is presented in Fig. 7. The gain is observed to vary between 7 and 40 across the EXFLU samples. The resulting signal amplitude at a given gain is largely invariant of substrate thickness, despite the dependence of thickness on the delivered charge.

The gain measured in the irradiated 30 μm sensors is susceptible to the change in temperature during data taking. Therefore, the charge collected is corrected by incrementing the reverse bias by 2 V per 1°C to obtain a bias range at a fixed temperature of -42°C [17]. The gain calculation for irradiated

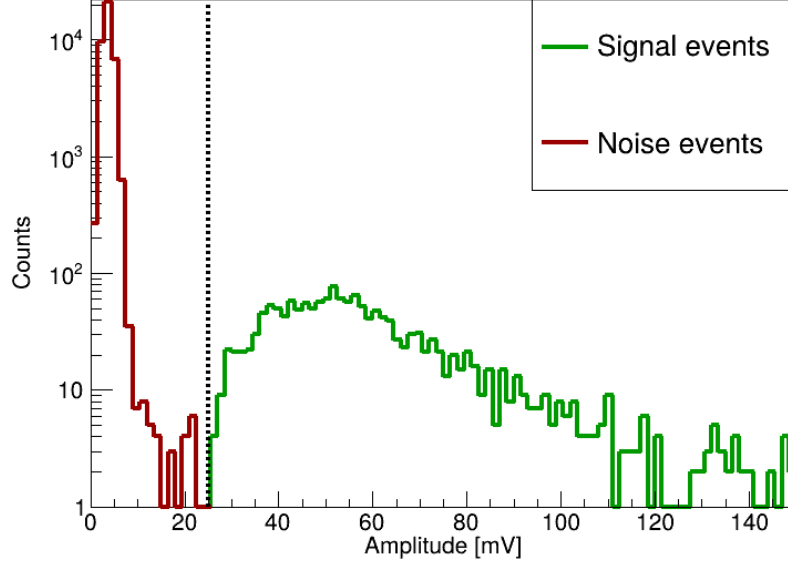


Figure 4: The distribution of signal amplitudes for the 20 μm CBL LGAD sensor under 150 V external bias at 18°C, with the selected signal events indicated above amplitudes of 25 mV. The shape is typical for all samples.

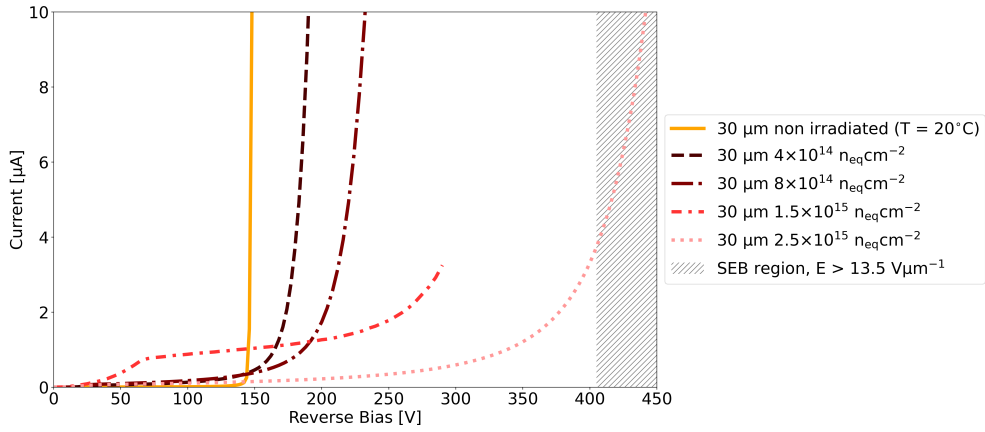


Figure 5: The breakdown curves for the irradiated 30 μm samples, performed at -20°C, highlighting the increasing breakdown with higher fluences due to the onset of acceptor removal. The SEB region is also shown here, above the 405 V threshold for 30 μm sensors.

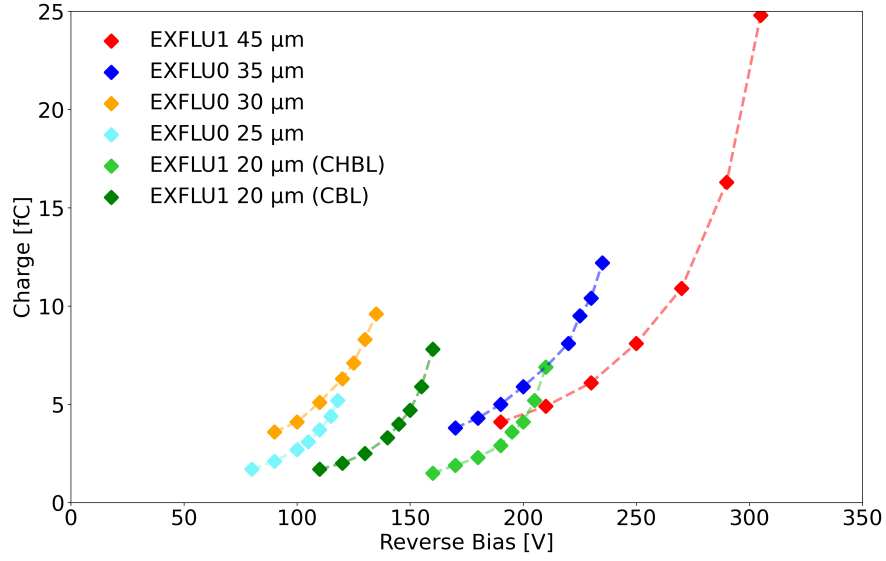


Figure 6: Charge injected into non-irradiated EXFLU samples as a function of the external bias, recorded at 18°C, ranging within 2 and 15 fC conditionally on thickness.

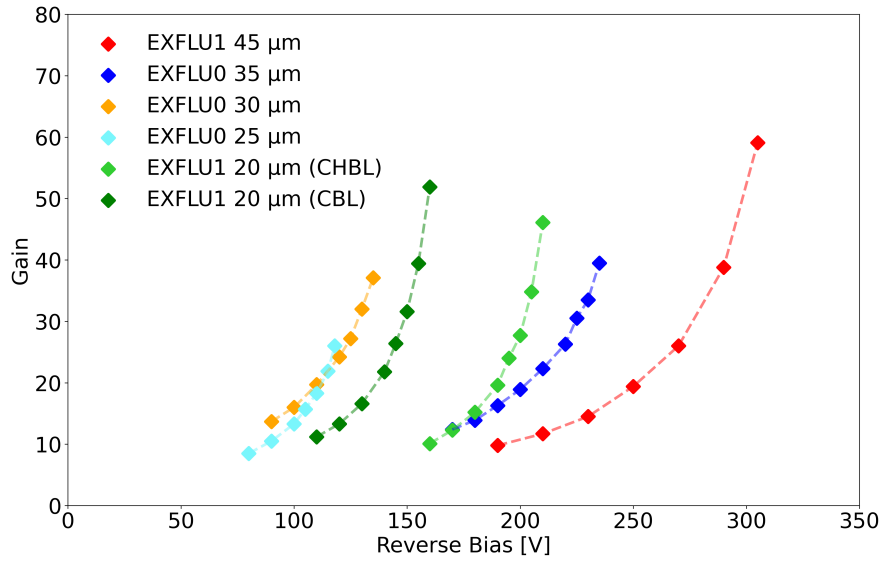


Figure 7: Gain measured in non-irradiated EXFLU samples as a function of the external bias, recorded at 18°C, ranging from 4 to 70 largely independent of thickness.

sensors similarly follows the calculation outlined in Ref. [20], however the estimation does not account for the inefficiency in charge collection due to trapping after irradiation.

The charge injected varies from 2 to 9 fC in sensors irradiated up to $1.5 \times 10^{15} \text{ n}_1 \text{ MeV eq. cm}^{-2}$, and between 2 and 4.5 fC in the sensor irradiated at $2.5 \times 10^{15} \text{ n}_1 \text{ MeV eq. cm}^{-2}$ at biases below the SEB limit. These correspond to a gain of between 10 and 30, and between 10 and 20, respectively, as demonstrated in Fig. 8 for charge values at the temperature the data was recorded, and in Fig. 9 for data corrected to -42°C .

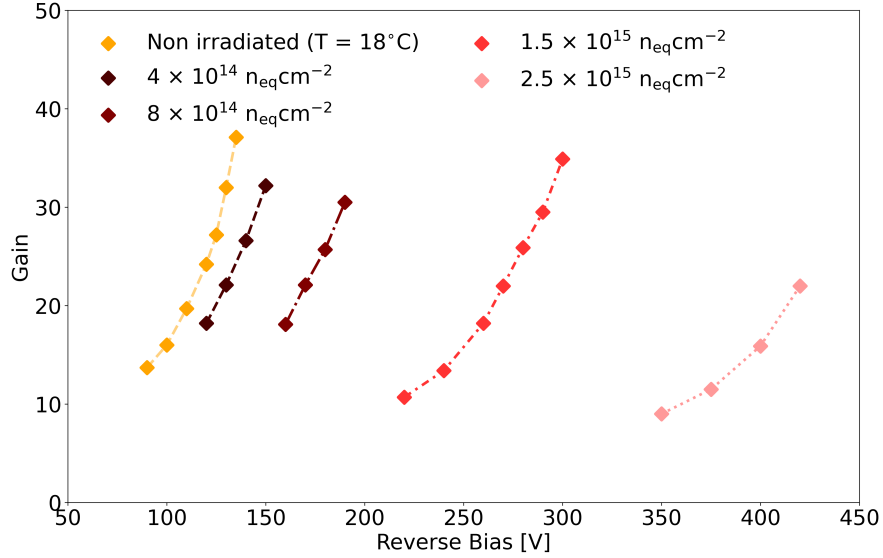


Figure 8: Gain measured in the 30 μm EXFLU samples as a function of the external bias, recorded at 18°C for the non-irradiated sample and between -50 and -42°C in the irradiated samples.

The t_{rise} of thin LGADs above the saturation threshold for electron drift velocity of $3 \text{ V}\mu\text{m}^{-1}$, taken at the 10%-90% interval, is observed to decrease from 600 to 300 ps linearly with the sensor thickness. This linear dependence is illustrated in Fig. 10, and is indicative of an intrinsically improved timing resolution in thinner LGADs. The noise is quantified as the root-mean-square of the signal baseline, and ranges from 1.2 to 1.5 mV in sensors thicker than 20 μm , and between 1.4 and 1.6 mV in the 20 μm samples.

The t_{rise} decreases marginally with fluence in the irradiated 30 μm sam-

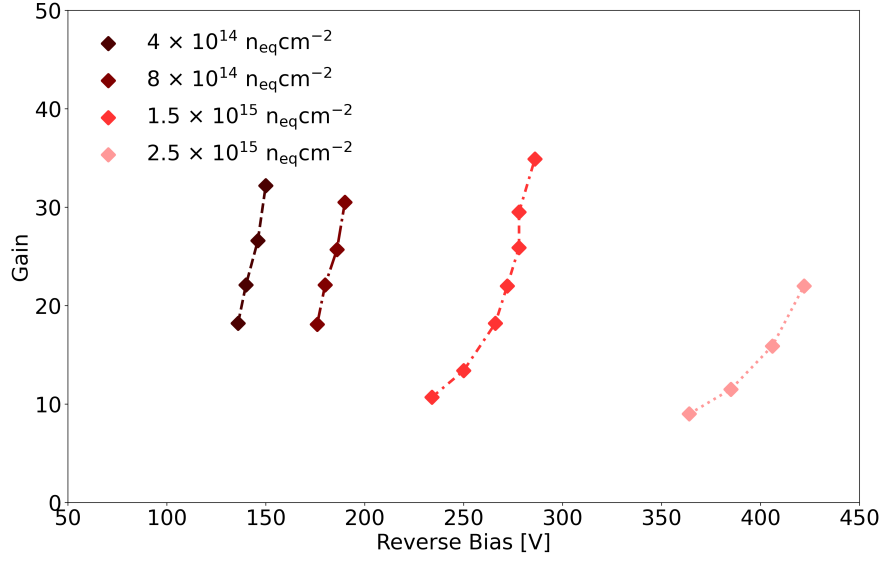


Figure 9: Gain measured in the irradiated 30 μm EXFLU samples as a function of the external bias, corrected to -42°C , The multiplication ranges from 10 to 30.

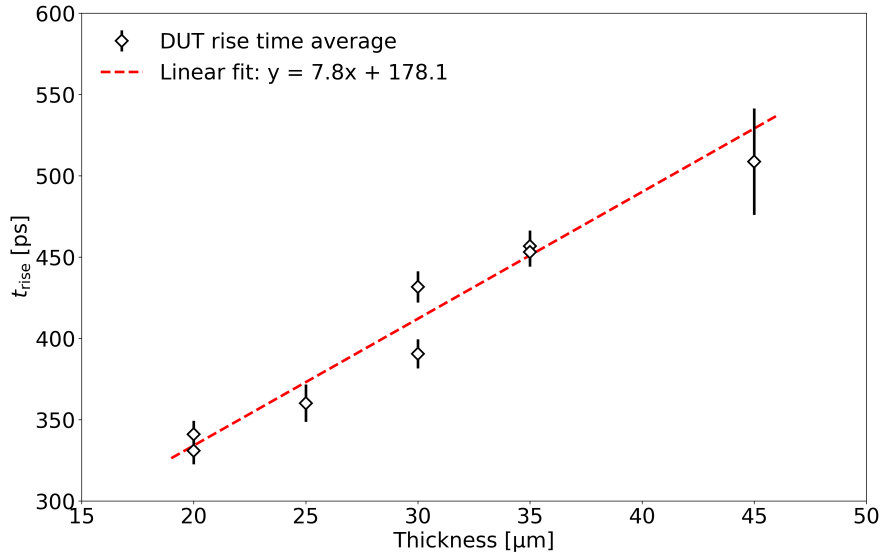


Figure 10: The t_{rise} of each EXFLU sample, taken at the 10%-90% interval, demonstrating a linear relationship with the thickness of the sensor.

ples, due to the increased bulk electric-field strength. This effect however is not as clear a trend as observed in the non-irradiated sensors. The root-mean-square noise in these samples is between 1.2 and 1.4 mV, apart from the sample irradiated at $1.5 \times 10^{15} \text{ n}_1 \text{ MeV eq. cm}^{-2}$ which reached 2.2 mV at the highest bias point, indicating an increase of the shot noise contribution.

To improve the quality of signal events, events are selected from the MCP as well as the DUT, requiring waveforms with amplitude above the trigger threshold of 40 mV but below electronic saturation of the oscilloscope, fixed at 540 mV. The sensitivity of the timing resolution to additional event selections was found to be negligible.

The timing resolution is calculated from the coinciding filtered DUT and MCP events using a constant fraction discriminator (CFD). The optimal thresholds were found to correspond to the time of arrival at the 30% level for all tested sensors. The distribution of the difference in CFD values from the DUT and MCP events is then fitted with a Gaussian formula, and the standard deviation of the fit is the timing resolution of the combined DUT-MCP system, $\sigma_t(\text{DUT}; \text{MCP})$. The timing resolution of the DUT, $\sigma_t(\text{DUT})$, is calculated from the quadrature difference:

$$\sigma_t(\text{DUT}) = \sqrt{\sigma_t^2(\text{DUT}; \text{MCP}) - \sigma_t^2(\text{MCP})}, \quad (1)$$

where $\sigma_t(\text{MCP})$ is the contribution due to the intrinsic timing resolution of the MCP. A $\sigma_t(\text{MCP})$ value of $5 \pm 2 \text{ ps}$ is extracted using the two non-irradiated $20 \text{ }\mu\text{m}$ sensors, as outlined in Section 3.2.

The statistical uncertainty on $\sigma_t(\text{DUT})$ calculated directly from the Gaussian fitting is $\lesssim 2\%$. The number of selected signal events in the calculation of $\sigma_t(\text{DUT})$, both for LP and SP devices, is sufficient that the statistical contribution is negligible in the overall uncertainty.

The most significant sources of uncertainty in the timing resolution measurement are systematic in nature. Namely, for very thin LGAD sensors, these include the electronic noise, or jitter, and the non-uniform energy deposition by ionising particles traversing the sensors [17]. The jitter contribution to the timing resolution, σ_{jitter} , is inversely proportional to the signal-to-noise ratio for a given slew rate. A smaller electronics bandwidth ensures lower noise. However, a higher slew rate, which minimises the jitter, requires a larger bandwidth. Given the intrinsic bandwidth of $\sim 1.4 \text{ GHz}$, the jitter is $\lesssim 10 \text{ ps}$ in sensors below $45 \text{ }\mu\text{m}$ and $\lesssim 20 \text{ ps}$ in the $45 \text{ }\mu\text{m}$ sample, shown in Fig. 11. The contribution due to deposition effects by ionising particles,

$\sigma_{\text{ionisation}}$, is invariant of the charge collected but is lower for thinner sensors. The value for $\sigma_{\text{ionisation}}$ can be estimated using a fit between the $\sigma_t(\text{DUT})$ and charge values for each DUT using the formula

$$\sigma_t^2(\text{DUT}) = a^2 + \left(\frac{b}{Q}\right)^2, \quad (2)$$

where Q is the charge, and a and b are constants determined by the fit. In this case, a corresponds to the $\sigma_{\text{ionisation}}$ term, and is observed to decrease from 25 ps for the 45 μm sample to 15 ps in the 20 μm samples, shown in Fig. 12. The results are corroborated by previous measurements of sensors with thicknesses ranging from 35 μm to 80 μm using the β setup, and are in good agreement with the predicted $\sigma_{\text{ionisation}}$ trend from Weightfield 2 simulations [21].

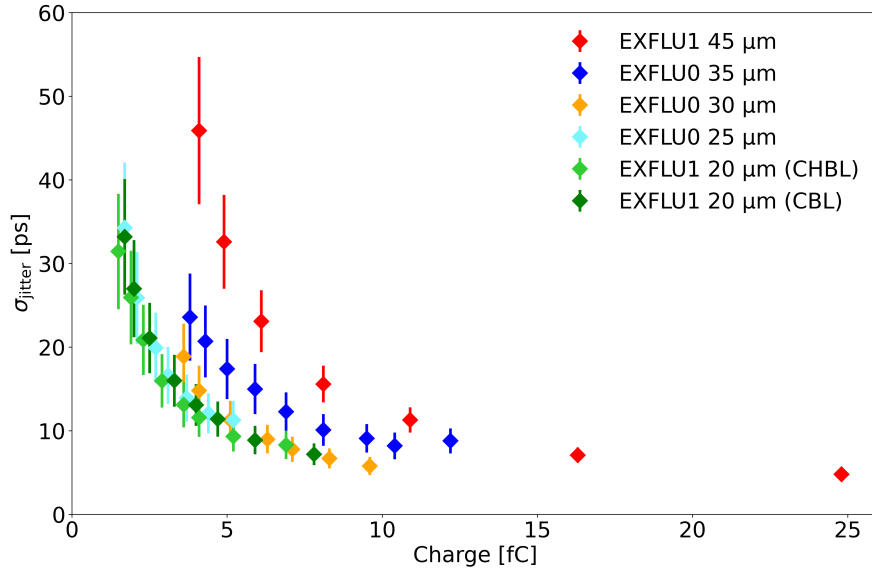


Figure 11: The σ_{jitter} contribution as a function of charge delivered by EXFLU samples. A sub-10 ps σ_{jitter} is achieved in all sensors of thickness below 45 μm .

Another significant systematic uncertainty is from the $\sigma_t(\text{MCP})$ measurement. The 2 ps uncertainty is a precise practical estimate using the samples available, given the low $\sigma_t(\text{MCP})$ of 5 ps. The uncertainties on the $\sigma_t(\text{DUT})$ estimates are nonetheless minimal, between 0.5 and 1.1 ps for the

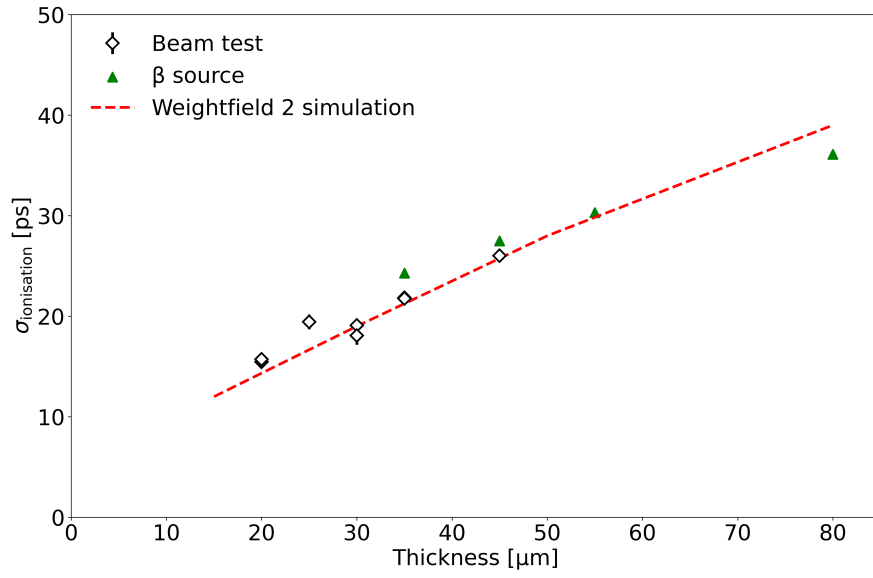


Figure 12: The $\sigma_{\text{ionisation}}$ contribution as a function of thickness using test beam data and from samples measured with a β source. The observations are in good agreement with the simulated $\sigma_{\text{ionisation}}$ behaviour using Weightfield 2.

non-irradiated samples, and between 0.7 and 0.8 ps for the irradiated samples. The 45 μm sample tested at the β setup has an uncertainty range of 0.8 to 1.5 ps.

A study was performed to estimate the systematic uncertainty in determining the signal amplitude due to the sampling rate of the oscilloscope, which directly affects the CFD. A large subset of signal data with amplitude within a 1 mV range was used. The functional form used to extract the amplitude was compared across different distributions, such as symmetric Gaussian, Lorentzian, parabolic, and Voigtian fits, and asymmetric Landau and skewed-Gaussian fits. The effect was found to be negligible on the overall timing resolution. Similarly, the mean of extracting the CFD value was compared between interpolating a data point via a linear fit to the two closest sampling points at the 30% threshold recorded by the oscilloscope, and using a spline fit along the rising edge of the signal shape. Again, there was no discernible effect on the timing resolution.

3.2. Intrinsic MCP timing resolution

The MCP timing resolution is computed using the data collected with the EXFLU 20 μm sensors. This assumes a tri-plane setup whereby the CFD value at 30% is measured for each pairing of planes, which gives the difference in time of arrival between each DUT and the MCP, as well as the difference between the two DUTs. The value for $\sigma_t(\text{MCP})$ is computed in this case using the equation

$$\sigma_t(\text{MCP}) = \sqrt{\sigma_t^2(\text{DUT1}; \text{MCP}) + \sigma_t^2(\text{DUT2}; \text{MCP}) - \sigma_t^2(\text{DUT1}; \text{DUT2})}, \quad (3)$$

where DUT 1 is the 20 μm CHBL sensor of higher operating bias, DUT 2 is the 20 μm CBL sensor of lower operating bias, and the terms above exploit the quadrature relations

$$\begin{aligned} \sigma_t^2(\text{DUT1}; \text{MCP}) &= \sigma_t^2(\text{DUT1}) + \sigma_t^2(\text{MCP}), \\ \sigma_t^2(\text{DUT2}; \text{MCP}) &= \sigma_t^2(\text{DUT2}) + \sigma_t^2(\text{MCP}), \\ \sigma_t^2(\text{DUT1}; \text{DUT2}) &= \sigma_t^2(\text{DUT1}) + \sigma_t^2(\text{DUT2}). \end{aligned} \quad (4)$$

The $\sigma_t(\text{MCP})$ value is estimated for multiple sets of data, given that DAQ was performed for several bias points, and an average timing resolution of 5 ± 2 ps is achieved.

4. Timing performance from test beam

The timing resolution $\sigma_t(\text{DUT})$ of all non-irradiated EXFLU samples studied at the Test Beam Facility is presented in Fig. 13 as a function of the injected charge, with the lowest measured value for timing resolution of each sensor thickness, $\sigma_t(\text{DUT})_{\min}$, given in Table 2. The values for $\sigma_t(\text{DUT})$ use the single-sensor plane method and Eq. 1, for a $\sigma_t(\text{MCP})$ of 5 ± 2 ps. The most evident trend is the effect of sensor thickness on $\sigma_t(\text{DUT})$, as predicted in the linear decrease in t_{rise} with substrate thickness highlighted in Fig. 10.

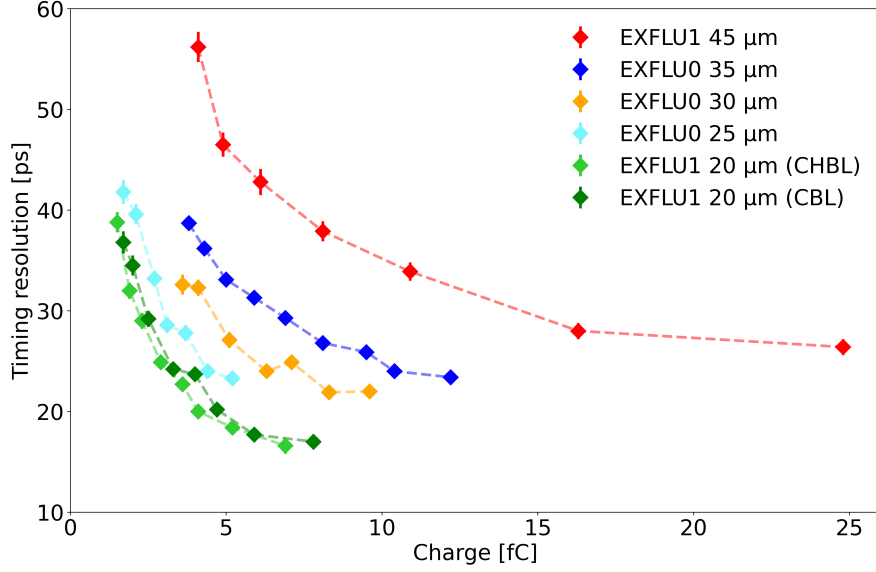


Figure 13: The $\sigma_t(\text{DUT})$ values across all non-irradiated EXFLU samples as a function of the charge injected, illustrating the effect of sensor thickness on timing precision. The 45 μm result is recorded using a β source.

The amount of injected charge required to reach a given $\sigma_t(\text{DUT})$ is also observed to decrease linearly and rapidly with the sensor thickness, illustrated in Fig. 14 with the charge uncertainties omitted. The data demonstrates that for a sub-30 ps $\sigma_t(\text{DUT})$, the minimum charge delivered is more than a factor of 2.5 times smaller between the 35 μm and 20 μm sensors, changing from ~ 6 fC to ~ 2 fC. The corresponding minimum charge for a 45 μm sensor is ~ 15 fC.

The timing resolution improves in a two-plane LGAD tracker setup using the 20 μm DUTs. By treating the time of the track as the average of the

Table 2: The lowest measured $\sigma_t(\text{DUT})$ value achieved for each non-irradiated EXFLU sensor thickness.

Thickness [μm]	$\sigma_t(\text{DUT})_{\min}$ [ps]
45	26.4 ± 1.7
35	23.4 ± 0.5
30	22.0 ± 0.7
25	23.3 ± 0.8
20	16.6 ± 0.7

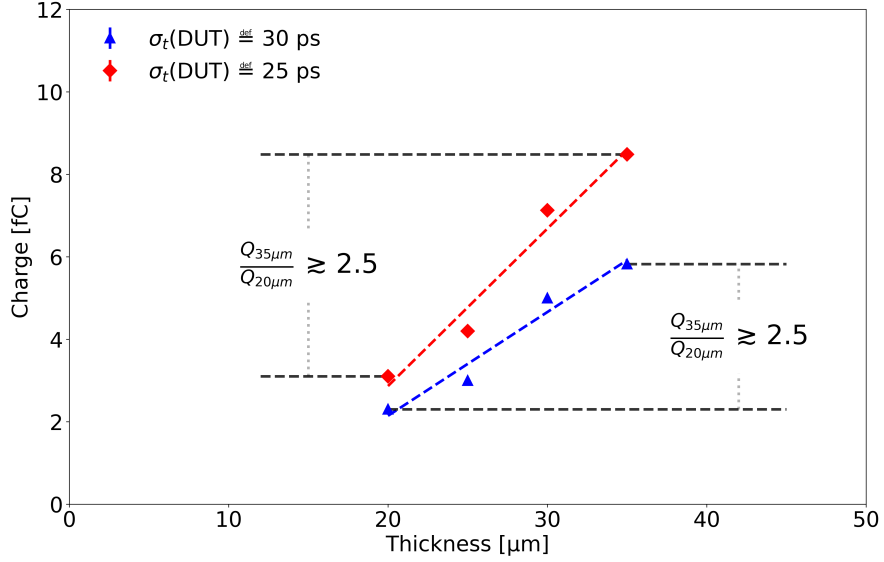


Figure 14: The minimum delivered charge required to achieve a fixed $\sigma_t(\text{DUT})$ value as a function of sensor thickness, highlighting the sensitivity between different EXFLU samples for a signal measured with a given precision. The uncertainties in the charge estimates are not shown.

times of arrival in each 20 μm DUT, a $\sigma_t(\text{DUT1}; \text{DUT2})$ of 12.2 ps is attained, minus the $\sigma_t(\text{MCP})$ contribution. The results of the two-plane setup for the 20 μm samples are shown against charge delivery in Fig. 15.

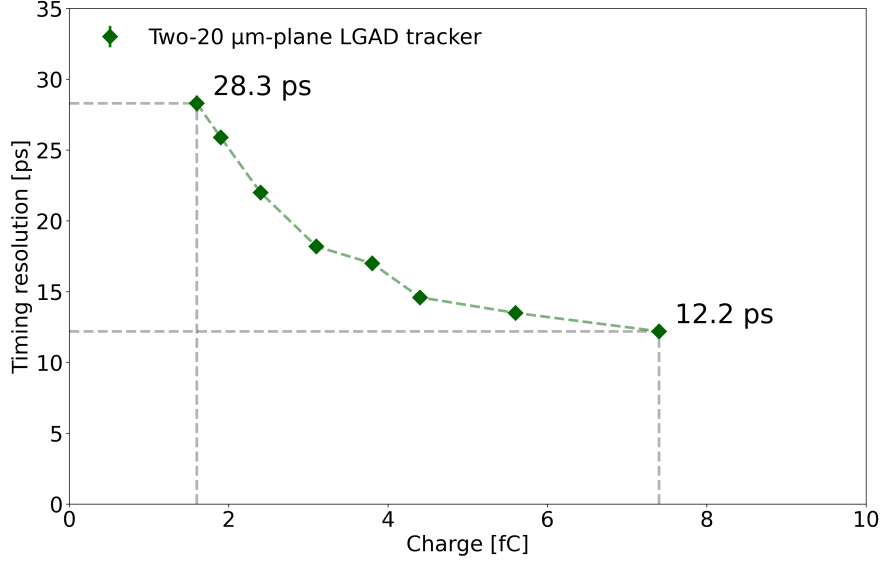


Figure 15: The timing resolution of a two-plane LGAD tracker setup with the 20 μm samples, where the average time of arrival of each DUT is used to compute the value for $\sigma_t(\text{DUT1}; \text{DUT2})$. The lowest $\sigma_t(\text{DUT1}; \text{DUT2})$ achieved in this setup is 12.2 ps.

In the irradiated samples, a timing resolution of 20 ps is achieved in all sensors irradiated up to $2.5 \times 10^{15} \text{ n}_1 \text{ MeV eq. cm}^{-2}$. The results are shown in Fig. 16 as a function of the external bias, and in Fig. 17 using data taken with irradiated samples at temperatures within the range of -50 and -42°C . The non-irradiated 30 μm sample is also shown here for reference, however the timing resolution is obtained at 18°C in this case, so is not directly comparable against the irradiated sensors operated at a lower bias due to the lower temperature conditions. The results of the $2.5 \times 10^{15} \text{ n}_1 \text{ MeV eq. cm}^{-2}$ indicate that a $\sigma_t(\text{DUT})$ of 20 ps is the best achievable outside of the SEB region [19]. The change in temperature does not significantly affect the $\sigma_t(\text{DUT})$ measurements, and hence no bias correction is applied.

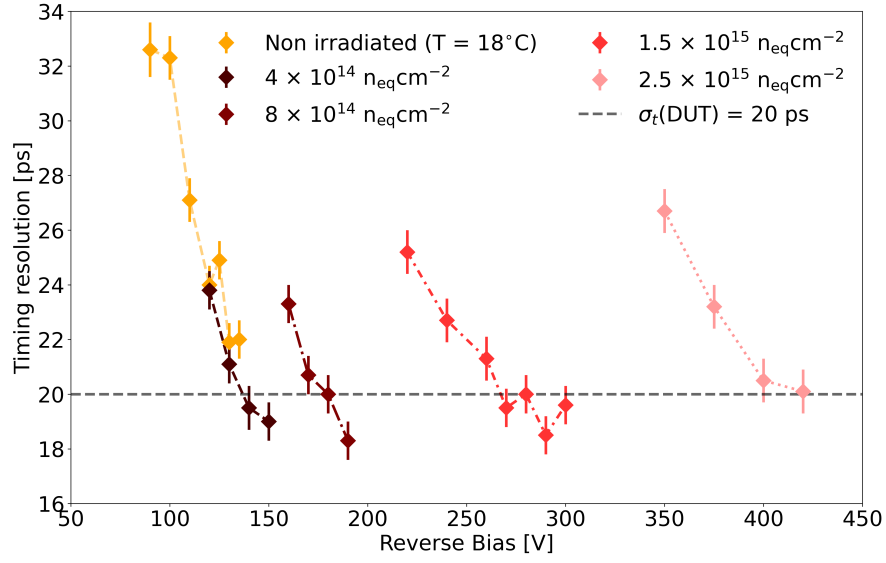


Figure 16: The timing resolution of the 30 μm sensors as a function of the external bias, using data obtained at temperatures within the range of -50 and -42°C for irradiated samples. The non-irradiated sample is tested at 18°C , and therefore operates at a higher bias. Even up to $2.5 \times 10^{15} \text{ n}_{\text{I MeV eq. cm}^{-2}}$ before reaching the SEB limit, a $\sigma_t(\text{DUT})$ of 20 ps is achieved in each irradiated sample.

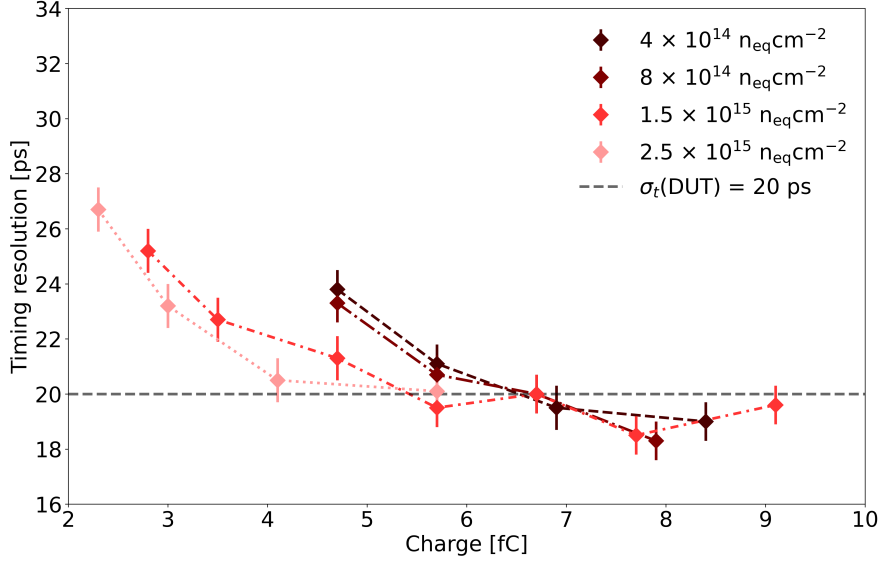


Figure 17: The timing resolution of the 30 μm sensors as a function of the charge injected, using data obtained at temperatures within the range of -50 and -42°C for irradiated samples.

5. Conclusion

The results of a test on a particle beam using 4 GeV/c electrons at the Test Beam Facility at DESY show that very thin EXFLU sensors with substrate thicknesses below 35 μm can achieve sub-25 ps timing precision, and as good as 16.6 ps in 20 μm sensors. A two-plane LGAD tracker setup using the 20 μm samples achieved a timing resolution of 12.2 ps. The improvement with substrate thickness is understood as the signal t_{rise} , and ionisation noise is inherently smaller for thinner LGADs. The minimum amount of charge required to achieve a given timing precision is also observed to decrease with active thickness. As expected, for a given gain the signal amplitude is observed to be independent of the substrate dimensions. Compared to contemporary fast ASICs, the performance of EXFLU sensors demonstrates a significant improvement with respect to the charge injection required to produce such timing precision. This is attributed to the EXFLU device having a thinner active substrate and hence higher capacitance. A study using irradiated 30 μm sensors demonstrated that a timing resolution of 18.3 ps is achieved for sensors irradiated at fluences up to $1.5 \times 10^{15} \text{ n}_1 \text{ MeV eq. cm}^{-2}$,

and 20.1 ps at $2.5 \times 10^{15} \text{ n}_1 \text{ MeV eq.cm}^{-2}$ before reaching the SEB limit. Minimal temperature effects manifest in the results for irradiated sensors due to data taking at temperatures between -50 and -42°C .

Acknowledgements

This project has received funding from the European Union’s Horizon 2020 research and innovation programme under Grant Agreements No 101004761 (AIDAInnova) and 101057511 (EURO-LABS), the European Union - Next Generation EU, Mission 4 Component 1 CUP D53D23002870001 (Comon-Sens), and the INFN CSN5 through the ‘eXFlu’ research project. The measurements leading to these results have been performed at the Test Beam Facility at DESY, Hamburg (Germany), a member of the Helmholtz Association (HGF).

References

- [1] L. Rossi, O. Brüning, High Luminosity Large Hadron Collider: A description for the European Strategy Preparatory Group, Tech. Rep. 236, CERN, Geneva (2012).
URL <https://cds.cern.ch/record/1471000>
- [2] A. La Rosa, The Upgrade of the CMS Tracker at HL-LHC, JPS Conf. Proc. 34 (2021) 010006. doi:10.7566/JPSCP.34.010006.
- [3] G. Aad, The ATLAS Upgrade for the HL-LHC, CERN (6 2025).
- [4] M. Benedikt, A. Chance, B. Dalena, D. Denisov, M. Giovannozzi, J. Gutleber, R. Losito, M. Mangano, T. Raubenheimer, W. Riegler, V. Shiltsev, D. Schulte, D. Tommasini, F. Zimmermann, Future Circular Hadron Collider FCC-hh: Overview and Status (2022). arXiv:2203.07804.
- [5] G. Pellegrini, P. Fernández-Martínez, M. Baselga, C. Fleta, D. Flores, V. Greco, S. Hidalgo, I. Mandić, G. Kramberger, D. Quirion, M. Ullan, Technology developments and first measurements of Low Gain Avalanche Detectors (LGAD) for high energy physics applications, Nucl. Instrum. Meth. A 765 (2014) 12–16. doi:10.1016/j.nima.2014.06.008.

- [6] M. Ferrero, A. Altamura, R. Arcidiacono, N. Cartiglia, M. Durando, L. Lanteri, C. Marinuzzi, L. Menzio, F. Siviero, V. Sola, R. White, FAST3 ASIC: an analog front-end with 30 ps resolution, designed to readout thin Low Gain Avalanche Diodes, *Journal of Instrumentation* 20 (03) (2025) C03007. doi:10.1088/1748-0221/20/03/C03007.
- [7] R. Padilla, C. Labitan, Z. Galloway, C. Gee, S. Mazza, F. McKinney-Martinez, H.-W. Sadrozinski, A. Seiden, B. Schumm, M. Wilder, Y. Zhao, H. Ren, Y. Jin, M. Lockerby, V. Cindro, G. Kramberger, I. Mandiz, M. Mikuz, M. Zavrtanik, R. Arcidiacono, N. Cartiglia, M. Ferrero, M. Mandurrino, V. Sola, A. Staiano, Effect of deep gain layer and Carbon infusion on LGAD radiation hardness, *J. Instrum.* 15 (2020) P10003. doi:10.1088/1748-0221/15/10/P10003.
- [8] A. Kolšek, V. Radulović, A. Trkov, L. Snoj, Using TRIGA Mark II research reactor for irradiation with thermal neutrons, *Nuclear Engineering and Design* 283 (2015) 155–161. doi:10.1016/j.nucengdes.2014.03.012.
- [9] M. Tornago, Performances of the latest FBK UFSD production, *Journal of Physics: Conference Series* 2374 (1) (2022) 012137. doi:10.1088/1742-6596/2374/1/012137.
- [10] V. Sola, Present and future development of thin silicon sensors for extreme fluences, Talk at VCI2022 – The 16th Vienna Conference on Instrumentation, Wien (Austria) (2022).
URL <https://indico.cern.ch/event/1044975/contributions/4663663/>
- [11] V. Sola, M. Boscardin, F. Moscatelli, A. Altamura, R. Arcidiacono, G. Borghi, N. Cartiglia, M. Centis Vignali, T. Croci, M. Durando, F. Ficorella, A. Fondacci, S. Galletto, G. Gioachin, S. Giordanengo, O. Hammad Ali, L. Lanteri, L. Menzio, A. Morozzi, D. Passeri, G. Paternoster, F. Siviero, M. Tornago, R. White, Thin LGAD sensors for 4D tracking in high radiation environments: state of the art and perspectives, *Front. Sens.* 6 (2025) 1648102. doi:10.3389/fsens.2025.1648102.
- [12] A. Altamura, R. White, M. Ferrero, L. Anderlini, R. Arcidiacono, G. Borghi, M. Boscardin, N. Cartiglia, M. C. Vignali, T. Croci, F. Davo-

- lio, M. Durando, A. Fondacci, S. Galletto, L. Lanteri, L. Menzio, A. Morozzi, D. Passeri, N. Pastrone, F. Siviero, F. Moscatelli, G. Paternoster, V. Sola, Radiation-resistant thin LGADs for enhanced 4D tracking, *Nucl. Instrum. Meth. A* 1081 (2025) 170799. doi:10.1016/j.nima.2025.170799.
- [13] R. Diener, J. Dreyling-Eschweiler, H. Ehrlichmann, I. Gregor, U. Kötz, U. Krämer, N. Meyners, N. Potylitsina-Kube, A. Schütz, P. Schütze, M. Stanitzki, The DESY II test beam facility, *Nucl. Instrum. Meth. A* 922 (2019) 265–286. doi:10.1016/j.nima.2018.11.133.
- [14] R. S. White, R. Arcidiacono, G. Borghi, M. Boscardin, N. Cartiglia, M. C. Vignali, M. Costa, T. Croci, M. Ferrero, A. Fondacci, S. Gordanengo, C. Hanna, L. Lanteri, L. Menzio, A. Morozzi, F. Moscatelli, R. Mulargia, D. Passeri, N. Pastrone, G. Paternoster, V. Sola, Characterisation of the FBK EXFLU1 thin sensors with gain in a high fluence environment, *Nucl. Instrum. Meth. A* 1068 (2024) 169798. doi:10.1016/j.nima.2024.169798.
- [15] M. Moll, Acceptor removal - Displacement damage effects involving the shallow acceptor doping of p-type silicon devices, *PoS Vertex2019* (2020) 027. doi:10.22323/1.373.0027.
- [16] M. Ferrero, Characterization of carbonated gain implants in Ultra Fast Silicon Detectors (UFSD) pre- and post-irradiation, Talk at TIPP2021 - The 5th Technology and Instrumentation in Particle Physics, Virtual (2021).
URL <https://indico.cern.ch/event/981823/contributions/4293561/>
- [17] M. Ferrero, R. Arcidiacono, M. Mandurrino, V. Sola, N. Cartiglia, An Introduction to Ultra-Fast Silicon Detectors, CRC Press, 2021. doi:10.1201/9781003131946.
- [18] G. Kramberger, V. Cindro, A. Howard, Z. Kljun, I. Mandic, M. Mikuz, Annealing effects on operation of thin Low Gain Avalanche Detectors, *J. Instrum.* 15 (2020) P08017. doi:10.1088/1748-0221/15/08/P08017.
- [19] M. Ferrero, R. Arcidiacono, N. Cartiglia, L. Lanteri, L. Menzio, A. Morozzi, F. Moscatelli, R. Mulargia, F. Siviero, R. White, V. Sola, First

- study of single-event burnout in very-thin planar silicon sensors, *Front. Phys.* 13 (2025) 1575672. doi:10.3389/fphy.2025.1575672.
- [20] S. Meroli, D. Passeri, L. Servoli, Energy loss measurement for charged particles in very thin silicon layers, *J. Instrum.* 6 (2011) P06013. doi:10.1088/1748-0221/6/06/P06013.
- [21] F. Cenna, N. Cartiglia, M. Friedl, B. Kolbinger, H. F. W. Sadrozinski, A. Seiden, A. Zatserklyaniy, A. Zatserklyaniy, Weightfield2: A fast simulator for silicon and diamond solid state detector, *Nucl. Instrum. Meth. A* 796 (2015) 149–153. doi:10.1016/j.nima.2015.04.015.